Icarus 426 (2025) 116365

Contents lists available at ScienceDirect

Icarus

journal homepage: www.elsevier.com/locate/icarus

Detection of lunar water, hydroxyl ion and their diurnal changes from CHACE-2 orbiter observation

Swastika Chakraborty [a,*], Barun Raychaudhuri [b], Tirtha Pratim Das [c], Saurabh Das [d], Moumita Roy [a]

[a] Narula Institute of Technology, West Bengal, India
[b] Presidency University, West Bengal, India
[c] Science Program Office, ISRO Headquarters, Bangalore, India
[d] Indian Institute of Technology, Indore, India

ARTICLE INFO

Keywords:
Lunar water
CHACE-2
Chandrayaan-2
Latitudinal map
Orbiter measurement

ABSTRACT

This work reports the spatial and diurnal variations of the number densities of lunar molecular water (H_2O), atomic mass unit (amu) 18 and hydroxyl (OH), amu 17 over low (0° to 30°), middle (31° to 60°) and high (61° to 80°) latitudinal regions of the lunar exosphere during the pre-sunrise, noon, sunset and midnight periods using the mass spectrometric data of CHandra's Atmospheric Composition Explorer-2 (CHACE-2) on board Chandrayaan-2, the second lunar mission developed in India. Both H_2O and OH exhibit, particularly in the low latitude regions, a trend of increasing number density after the sunrise and up to noon, followed by a decrease till sunset. An overall higher density of H_2O is obtained compared to the previous reports. The findings are justified in terms of the polar orbital height of the instrument and the duration of data procurement. The maximum number density for the low, middle and high latitudes reaches 5225 cm^{-3}, 5135 cm^{-3} and 3747 cm^{-3}, respectively. The corresponding OH abundances are found to be 5079 cm^{-3}, 5565 cm^{-3} and 5720 cm^{-3}. The diurnal variations of H_2O and OH and their comparisons, similar to those of the present report may provide suitable means for tracing the lunar water cycle. The CHACE-2 observations imply that the influence of magnetotail passage on volatiles like water is to be further quantified in future missions with other sensors.

1. Introduction

The quest for the existence of water in the Moon has been a subject of significant attention since the days before the lunar expeditions (Watson et al., 1961a; Watson et al., 1961b). The presence of water within the lunar regolith may be of interest looking towards future lunar habitats (Benaroya, 2017). Although Apollo and Luna missions found the lunar surface generally anhydrous (Shearer et al., 2006), the recent lunar missions and orbital observations have detected the presence of water or hydrated compounds in the Moon.

The Moon Mineralogy Mapper of Chandrayaan-1 detected at high latitudes (Pieters et al., 2009) and at all latitudes (Li and Milliken, 2017; Wöhler et al., 2017) and the Imaging Infrared Spectrometer on board Chandrayaan-2 detected at all latitudes (Chauhan et al., 2021) radiation absorption features around 2.8 to 3.0 μm, which provided evidence of hydroxyl or water-bearing materials. Evidence of water-ice abundances in the permanently shadowed lunar craters was reported (Colaprete et al., 2010). The ultraviolet albedo and temperature measurements from Lunar Reconnaissance Orbiter (LRO) detected the existence of water ice near the lunar south polar regions with heterogeneous distribution of exposed or mixed state with regolith and also suggested the presence of carbon dioxide ice (Hayne et al., 2015). Ultraviolet measurements of LRO also revealed the abundance of lunar surface water at mid-latitude (30°N -50°N) mare and highland regions, varying with terrain type, local time and temperature (Hendrix et al., 2019). Terrestrial airborne infrared observations of Stratospheric Observatory for Infrared Astronomy (SOFIA) revealed the presence of molecular water on the sunlit lunar surface, mostly at high latitudes (Honniball et al., 2021).

Considering all the above, a consensus may be established regarding the presence of varying amount of water in some form or other within the lunar surface. Nevertheless, opinion differs regarding the potential

* Corresponding author.
E-mail addresses: swastika.chakraborty@nit.ac.in (S. Chakraborty), barun.physics@presiuniv.ac.in (B. Raychaudhuri), tpdas.isro@gmail.com (T.P. Das), saurabh.das@iiti.ac.in (S. Das), moumitaroy0015@gmail.com (M. Roy).

https://doi.org/10.1016/j.icarus.2024.116365
Received 15 March 2024; Received in revised form 25 October 2024; Accepted 29 October 2024
Available online 31 October 2024

sources contributing to this lunar surficial and exospheric water inventory and its spatial distribution. The analysis of the data procured by Visual and Infrared Mapping Spectrometer (VIMS) on Cassini detected trace hydroxyl that suggested migration of water to polar region (Clark, 2009). The outgassing of volatiles through the regolith is suggested as a potential source of hydration (Crotts and Hummels, 2009). The observations executed by the Neutral Mass Spectrometer on board the Lunar Atmosphere and Dust Environment Explorer (LADEE) detected a water cycle involving the release of near-surface water into the exosphere, which was correlated with meteoroid impacts (Benna et al., 2019). An inward diffusion of solar wind-derived water is inferred from lunar soil extracts (Huicun et al., 2023).

The reported quantifications of lunar surficial and exospheric water also differ widely. According to the first global surface water (OH and H_2O) map (Li and Milliken, 2017), the surface abundance variation is ~200 ppm over a lunar day with an assumption of particle diameter of 60 to 80 μm. The report suggested a global average of $\sim 1.2 \times 10^{14}$ g of water contained within the upper meter of regolith. They found ~200–700 ppm of water content in the lunar surface having an increase with latitudes and suggested two different water reservoirs: a high latitude bulk content up to meters deep regolith that is stable over diurnal cycle and a low latitude surficial water content within 100–200 nm of outer regolith that undergoes diurnal variation under regolith and solar wind interactions. Benna et al. (2019) suggested a median density of 22.8 cm^{-3} for exospheric water (H_2O and OH) molecules with median absolute deviation of 11.3 cm^{-3}. Hendrix et al. (2019), using Lyman Alpha Mapping Project data, estimated about 400 cm^{-3} of water molecules at an altitude of 50 km assuming that water vapor remains intact when it repeatedly strikes the lunar surface. As per the report of Cassini space probe (Clark, 2009), 10 to 1000 ppm of water is detected by Visual and Infrared Mapping Spectrometer, which depends on the grain size and the type of mixing of rocks and soils. Later, a lower limit of 320–820 ppm of H_2O in KREEP type rocks was estimated from hydrogen enhancement statistics (Lawrence et al., 2022). Mean H_2O abundance of about 250 μg g^{-1} in lunar south polar region was estimated from SOFIA measurement (Honniball et al., 2022).

The loss of hydration and its recovery from the lunar surface between the sunrise and sunset terminators is a dynamic process and it is the indication of lunar exospheric water cycle. Therefore, the diurnal variation of lunar water content has a great significance in understanding the lunar water cycle, which is still a matter of exploration. This work reports the detectability of the diurnal changes of lunar exospheric water molecules and hydroxyl ions from CHACE-2 orbital observations. This may be useful to investigate the trends of variation of water abundance on and around the Moon.

2. Materials and method

This work analyzes the mass spectrometric data of the lunar exosphere procured by CHandra's Atmospheric Composition Explorer-2 (CHACE-2), one of the instruments of the second Indian lunar mission named Chandrayaan-2 launched on July 22, 2019. The orbiter was installed in near circular polar orbit at an average altitude of 100 km with a range of variation of 80–120 km. CHACE-2 started recording data since September 2019 at different local time of noon-to-midnight and sunrise-to-sunset. The data provider's archive (https://pradan.issdc.gov.in/pradan/) was accessed on Nov. 17, 2023 and the downloaded data were sorted and arranged for the low, mid and high latitudes for different solar times.

2.1. The CHACE-2 instrument

The CHACE-2 instrument (Das et al., 2020) on board Chandrayaan-2 is a successor of CHandra's Altitudinal Composition Explorer (CHACE) on Moon Impact Probe of Chandrayaan-1 mission (Sridharan et al., 2010; Das et al., 2016; Das et al., 2017) and the Mars Exospheric Neutral Composition Analyzer (MENCA) on board Indian Mars Orbiter Mission (Bhardwaj et al., 2015). CHACE-2 is a mass spectrometer capable of distinguishing ions of different mass-to-charge (m/q) ratio under electric field. The experiment is to be conducted under high vacuum that is naturally available in the lunar exosphere. The instrument has three major components, namely an ion source, a quadrupole mass analyzer (QMA) and an ion detector.

The ion source is an open-source hot-cathode electron impact ionizer that generates thermionic electrons accelerated to about 70 eV (adjustable as per requirement) for ionizing the exospheric ambient neutrals. A fraction of the total emission current from the ionizer filament is used in ionizing the neutrals within the ionizer source grid (basically a Faraday Cage). The ions thus generated are focussed towards the QMA. The other part of the current ionizes the neutrals outside the grid and the ions generated are collected by a Bayard-Alpert (B-A) gauge, suitable for measuring pressure less than 10^{-4} Torr. The B-A gauge measures the total pressure that corresponds to the absolute abundance of the constituents. The gauge is ground-calibrated under nitrogen-rich environment of known pressures.

The QMA is comprised of two pairs of electrically connected, diametrically opposite cylindrical rods, each of ~15 cm length and ~ 1 cm diameter. Each pair is supplied with a potential having static (DC) component and radio frequency (RF) component (~ 2.3 MHz) superimposed to each other. The pairs have 180° phase difference for the RF part. The ingested ion beam may contain ions of various m/q ratios. However, for a given DC-RF amplitude ratio, only a particular species of specific m/q ratio can reach the detector in a stable path. Others undergo unstable oscillations and strike the rods. Thus, changing the DC-RF ratio, the QMA can be acted as a 'mass filter'. The mass range is 1–100 amu or 1–300 amu with unit mass resolution, programmable through telecommand. A complete scan for 1–100 amu takes about 38 s and an algorithm corrects for the actual mass position in the spectra (Dhanya et al., 2023). The present work has used the 1–100 amu mass range.

The ion detector is a combination of a Faraday cup and a Channel Electron Multiplier (CEM), suitable for pressures less than 10^{-7} Torr. The CEM has a gain of $\sim 10^5$ for a bias voltage of ~2000 V. The CEM detector is ground-calibrated at high vacuum ($\sim 2 \times 10^{-11}$ Torr) under He, Ar, N_2 and Xe gas environments. The ion motion depends on its mass, the DC and RF amplitudes and the RF frequency but is independent of the initial conditions. All the ions having these parameters alike have the same periodicity of motion. Assuming all single-ionized species, the m/q variation constitutes the mass axis (abscissa) and the ion current recorded for an individual species forms the partial pressure axis (ordinate) of the mass spectra. The total emission current gets stabilized in about 12 s, and this is sufficient for measuring the relative abundances of the species. Nevertheless, the absolute partial pressure measurement requires the stabilization of the ratio of the two fractions of the current, namely the B-A gauge component and the QMA component, which takes about 22 min. The instrument is to be kept on for at least this duration. In practice, the observations are recorded after 30 min of the time of switching on.

Instruments like CHACE-2 are generally power-consuming devices. The overall power consumption in the spacecraft necessitates the limiting of the duration of operation of CHACE-2. Also, the 'thermal management' of the system involving the radiative heat exchange, the uniformity of heat distribution and a fixed chassis temperature is an important factor. Considering these all, the duration of operation of CHACE-2 was initially (up to the middle of year 2020) limited to a single orbit of Chandrayaan-2 around the Moon taking two hours of time. Subsequently it was increased to four hours of operation. Since the pressure of the open ionizer remains the same as that of the surrounding vacuum, the accumulation on the chamber walls and the reactions taking place are minimized so that the H_2O and OH can be distinctly identified from the mass resolution.

Table 1 presents a comparison of the technical specifications of CHACE-2 onboard Chandrayaan-2 with those of the Neutral Mass

Table 1
Comparison of the technical specifications of CHACE-2, Chandrayaan-2 and NMS, LADEE (Elphic et al., 2014; Mahaffy et al., 2014; Benna et al., 2019; Das et al., 2020).

PARAMETER	CHACE-2, Chandrayaan-2	NMS, LADEE
Scan range	1–100 amu or 1–300 amu, programmable by telecommand	2–150 Da
Scan Resolution	1 amu	1 amu or 0.1 amu (optional)
Ion source	Single open-source hot-cathode ionizer	Two separate closed- and open-source ionizers
Mass filter type	Quadrupole	Quadrupole
Detector	Faraday cup and channel electron multiplier (CEM) for partial pressure and Bayard-Alpert (B-A) gauge for total pressure	Ion focusing lenses and CEM for partial pressure and Bayard-Alpert (B-A) gauge for total pressure
Payload mass	3.73 kg	11.8 kg
Power budget	33 watt	34.4 watt
Overall dimension	235 mm (L) × 108.7 mm (B) × 372 mm (w)	432 mm (L) × 245 mm (B) × 370 mm (w)
Spacecraft position	Nearly polar orbit of ~100 km altitude from the lunar surface. Orbiting time of 2 h.	Nearly equatorial orbit of varying altitude (~ 60–4 km). Orbiting time less than 2 h.
Orientation of operation	The instrument orientation is tracked by recording the roll angle with respect to the roll-axis of the spacecraft.	Separate modes for (i) ram and (ii) anti-ram directions of the spacecraft, (iii) tilted 30° off-ram and (iv) along the normal to the elliptic path.
Data acquisition	Typical activity for 2–6 h, 4 or more operations per day. Time spared for initial stabilizations before measurement ~30 min. The present work avoided the initial 1 year data and utilized the subsequent 2 years data.	Typical activity for 30–60 min, initially 5 and finally ~20 operations per day. Time spared for initial stabilizations before measurement ~2 min. The whole data acquisition period was less than 1 year.
Mission Duration	Launched in July 2019. Procured science data for almost four years.	Launched in Sept., 2013. Science phase continued for 100 days.

Spectrometer (NMS) onboard LADEE mission. It is noted from the table that CHACE-2 has an advantage of extended time span of nearly four years compared to several months of LADEE NMS for the scientific measurements. Also, CHACE-2 is in a convenient state for settling down and minimizing the outgassing effect over a long duration.

2.2. The spacecraft outgassing

Space-borne mass spectrometers may get contaminated by the outgassing of molecules at low pressure, particularly desorption of water from their own components, such as insulation, electronic circuits and optical surfaces. Such outgassing poses a major disturbance to the mass spectrometric measurement of volatiles like water in lunar exosphere and similar tenuous atmospheres. The prime processes contributing to outgassing are diffusion, desorption and decomposition where the decomposition is independent of time but the diffusion and desorption processes are functions of time and temperature. As the time of measurement increases, the process of desorption decreases exponentially and the diffusion process is inversely proportional to the square root of time. The partial pressure of outgassed water and other contaminants are reported to be of the order of 10^{-11} mbar or less (Schläppi et al., 2011).

Consistent with the above features of outgassing, the total pressure estimated by CHACE-2 got reduced and stabilized after more than one year since the initial onboard days, as shown in Fig. 1. In course of the orbiting motion, one end of the spacecraft rams into the exospheric molecules and the other end leaves a wake behind, which are quantified in terms of the roll angle. Fig. 1 shows the mean values of total pressure estimated in the ram direction (roll angle 0° to 45°) and in the anti-ram direction (roll angle 135° to 180°), respectively, for different months since the initial onboard days of CHACE-2. It estimates a persistent outgassing background that can be minimized but can never be removed. Although the range of outgassing pressure is negligible compared to the total signatures of lunar volatiles, the total pressure in anti-ram direction ($\sim 10^{-9}$ Torr) was subtracted from that in the ram direction ($\sim 10^{-7}$ Torr) to obtain the actual pressure.

2.3. Data processing

As mentioned earlier, the data collected by CHACE-2 are in the form

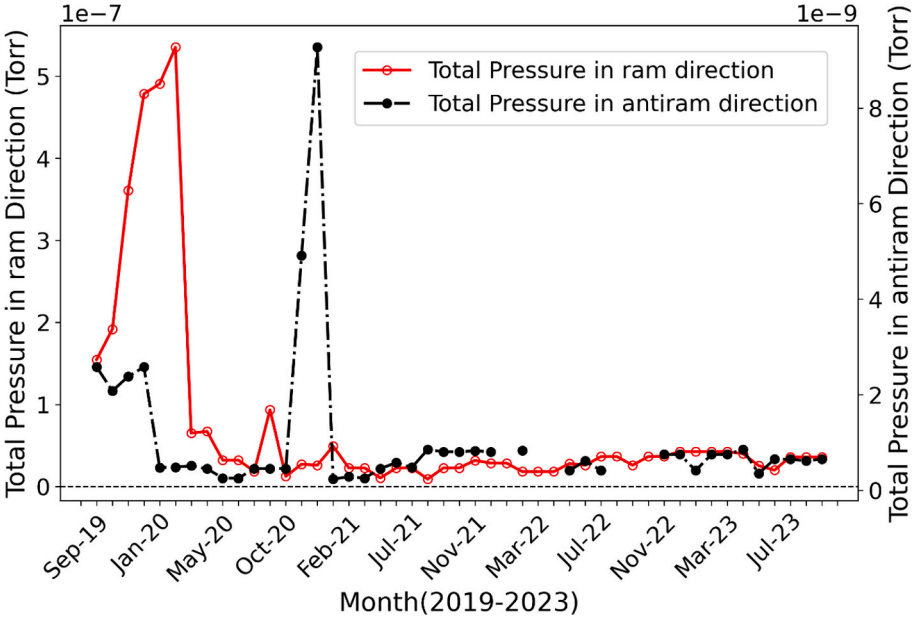

Fig. 1. Variation of total pressure along ram and anti-ram directions since the initial onboard days of CHACE-2.

of raw partial pressures for different exospheric species of different atomic mass unit (amu). During the initial days of the mission, the mass spectra of CHACE-2 might be contaminated by outgassing thereby abruptly changing the recorded partial pressure. This problem of pressure fluctuation was gradually stabilized after December 2020. The present work has considered only the sets of data procured after the stabilization of the total pressure. Analyses of the spatial and temporal variations of molecular water (H_2O, amu 18) and hydroxyl (OH, amu 17) were carried out separately. The following corrections were made to the raw values of partial pressure.

In order to minimize the ram enhancement effect, the data corresponding to the roll angle of the spacecraft less than 45° were considered for the analysis. A correction term $[v_s cos(\alpha) + v_{th}]/v_{th}$ for the roll-angle (α) of the spacecraft was incorporated by the data provider (https://pradan.issdc.gov.in/pradan/), the spacecraft velocity (v_s) being available at the software toolkit named SPICE provided with the data archive. Here v_{th} is the thermal velocity of the exospheric species. The available raw pressure values were divided by the correction factor mentioned above. A typical way of ingestion of exospheric neutrals accommodated to the surface temperature is sketched in literature (Sarantos et al., 2012).

An effective volume enhancement occurs due to the volume swept by the entrance aperture of the moving mass spectrometer during the time that a sample is ingested. The need of a correction for such volume enhancement is mentioned in previous reports (Sridharan et al., 2015; Das et al., 2016; Dhanya et al., 2021). The volume enhancement correction for the present data were calculated as follows. CHACE-2 is orbiting with Chandrayaan-2 with a velocity of $v = (GM/r)^{1/2}$ at an altitude of about 100 km over the surface of the Moon. Assuming the gravitational constant $(G) = 6.6743 \times 10^{-11}$ Nm^2kg^{-2}, the mass of the Moon $(M) = 7.34767 \times 10^{22}$ kg, the radius of the Moon $(R) = 1737.4$ km and $r = R + 100$, the orbiting velocity (v) is calculated as 1.6 kms^{-1} approximately. The length of the quadrupole mass filter rods, hence the ionic path length was of centimetre order but by virtue of the spacecraft velocity, it traversed about 1.6 km ($= 1.6 \times 10^5$ cm) in a second and the effective volume for ionization increased by this factor. Therefore, the recorded raw pressure values were divided by 1.6×10^5 to obtain the corrected pressure. During the ~38 s of mass scan, the spacecraft, with its speed of ~1.6 km per second, moves through ~60.8 km. Assuming a spherical Moon, this distance is comparable to a lunar longitude and is less than a lunar latitude. Thus, a specific measurement may be considered as a local feature specified by the latitude-longitude position.

Fig. 2 shows the relevant components of sample mass spectra for a range of 1 to 100 amu for ram as well as anti-ram direction. The presence of amu 17 and 18 are pointed out in the figure. There exist, of course, the signatures of many other species. For instance, Dhanya et al. (2021) estimated Argon-40 in lunar exosphere using the same CHACE-2 data. However, the present work concentrates on the two entities only: H_2O and OH and the attempt to explore other features might be a different venture. The partial pressure values along the anti-ram direction (~10^{-11} Torr) were consistently subtracted from the corresponding partial pressure value along the ram direction (~10^{-9} Torr) in order to minimize the effect of outgassing while calculating the H_2O (amu 18) and OH (amu 17) abundance from their partial pressure.

Fig. 3 shows the step-by-step algorithm for calculating the partial pressure for each of H_2O and OH. Two correction factors are already incorporated by the data provider to the available raw partial pressure data accounting for the difference of transmission efficiencies of the QMA for lighter and heavier ions and the gain of the CEM, respectively. The roll angle correction and the volume enhancement correction, as mentioned above in detail, were executed along with the work. The temperature required for the calculations were estimated in the following way (Hurley et al., 2015; Williams et al., 2017). The Diviner observed temperature is approximated by two different analytic functions, one for dayside and the other for nightside up to the terminator. The dayside temperature is represented by Eq. (1), a cosine function of solar zenith angle (ψ), the angle between the vector from the Moon centre through the lunar surface point and the Moon-Sun line (Hurley et al., 2015).

$$T(\psi) = T_0 cos^n(\psi) + T_1 \qquad (\psi < 90^\circ) \tag{1}$$

T_0 is taken as 262 K, T_1 as 130 K, and n is considered as $\frac{1}{2}$ matching with Diviner measurements. The nightside temperature is approximated by Eq. (2), a 6-term polynomial function of longitude (φ) and colatitude (θ) (Hurley et al., 2015).

$$T(\theta, \varphi) = \sum_{i=0,\ldots,5} \left(a_i \varphi^i + 35(sin(\theta) - 1) \right) (\psi > 90^\circ) \tag{2}$$

where the six values of a are 444.738, −448.937, 239.668, −63.8844, 8.34064 and − 0.423502. The ideal gas equation is followed for estimating the number density from the corrected partial pressure using the calculated temperature.

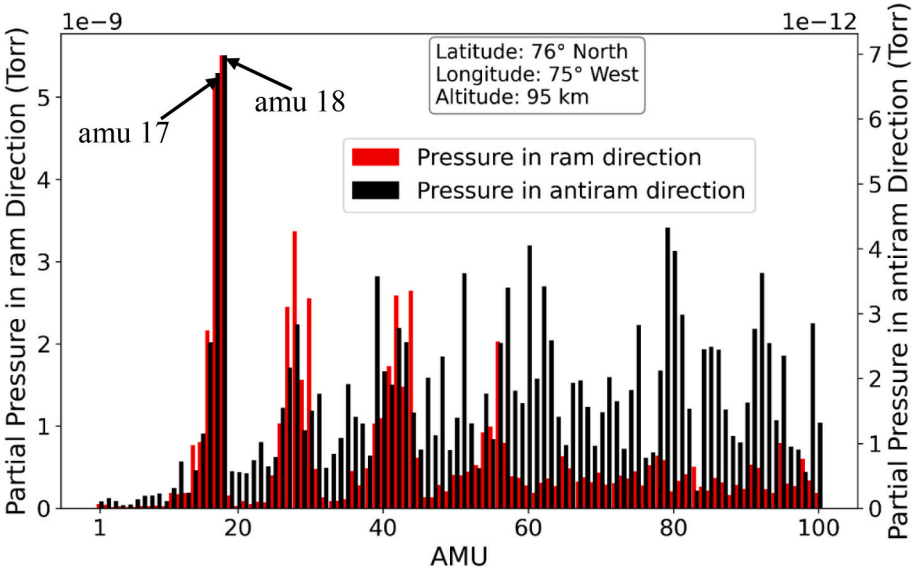

Fig. 2. Sample spectra showing the presence of amu 17 and 18. There are indications of the existence of other species but those are not the focus of present study.

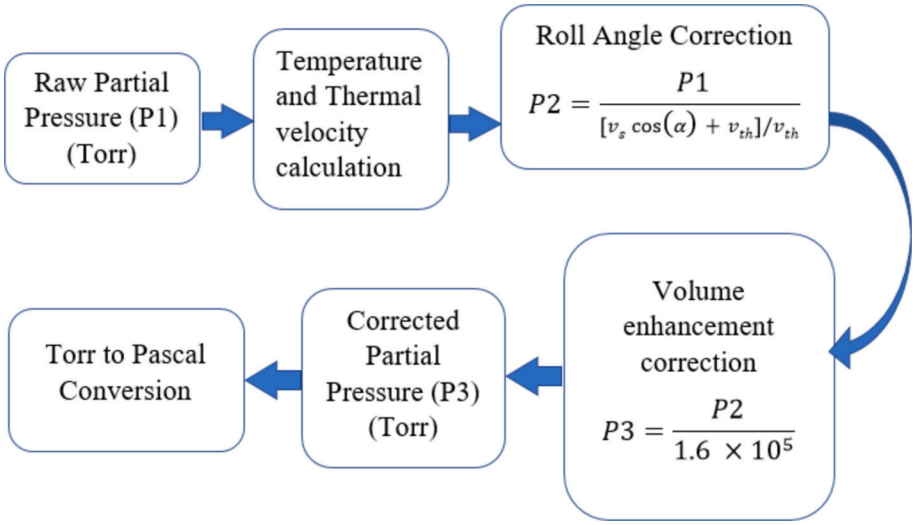

Fig. 3. Data processing algorithm steps for calculating the partial pressure for H_2O and OH.

3. Latitudinal and diurnal observations and results

The polar orbital movement of CHACE-2 has the advantageous feature of observing the local time dependence of the lunar exospheric species. This section explores the partial pressure data collected for different latitudinal zones at different solar longitudes and at varying local solar time. The Moon is a slow rotator and thereby it is assumed to keep up a radiative equilibrium. As a consequence of that, the radiation flux varies diurnally and can be approximated from bolometric brightness temperature.

3.1. Low latitude regions

Fig. 4(a) displays the diurnal variations of H_2O and OH abundances for a typical low latitude range (0° to 30° for both hemispheres). It is visible that the number density (cm^{-3}) of both H_2O and OH fluctuate over a big span, ranging from a few (similar to Benna et al., 2019) to few thousands cm^{-3}. For a particular solar longitude, the mean values are represented by dots and the ranges of fluctuation are drawn as lines. The most prominent and regular finding is the rapid enhancement of H_2O number density after the sunrise, continuing up to noon and then decrease of the same with sunset. Such observations may be treated as a typical feature of a condensable gas. For the night time, there is an overall decreasing tendency of H_2O concentration but some discrete higher values of both H_2O and OH are noted after sunset. The interesting one is the diurnal variation of OH, which shows an increasing tendency like that of H_2O after sunrise but exhibits a relatively higher abundance after sunset also.

The above results are partly consistent with the chemical kinetic model for the balance of formation and loss of OH in lunar regolith (Jones et al., 2018). Following the same, one can state that the oxygen atoms present within the regolith react with the solar wind protons to form OH groups at high temperature at the sunlit lunar surface. The OH, by desorption, can form molecular H_2O, which release in ballistic trajectory with thermal velocity, partly re-adsorb and partly photodissociate in presence of sunlight (ultraviolet) to form OH and H radicals. Some of these escape the gravitational attraction, and some others with less energy impact the surface and get adsorbed into the regolith. Recombinative desorption could also be responsible for the observed enhancement at noon (Jones et al., 2024).

Fig. 4(b) revisits the expected local time dependence of lunar exospheric condensable (e.g. Ar) and non-condensable (e.g. He) species by collecting some results from literature. Following a similar trend, the density of H_2O should have been decreased during night time, which is not obtained with the present results of Fig. 4(a). At present, no existing exosphere model predicts the observed local time dependence of H_2O at night. A possible interpretation is put up in the following way. Lunar surface temperature increases rapidly after sunrise, releasing more H_2O molecules in the exosphere for photodissociation. However, the temperature decrease due to the cooling process after sunset is likely to be slower. Recently it is put forward that a microscale system not in thermodynamic equilibrium heat up faster than cooling down (Ibánez et al., 2024). Such asymmetry, if applicable to exospheric molecules, may keep the H_2O molecules and OH radicals sustained in the exosphere even after the sunset. The OH is not volatile/condensable of its own like the molecular water. Also, the chance of photoexcitation and combining of OH into molecular H_2O is negligible at night time. These give some potential reasons for the presence of higher OH density after sunset. Schörghofer et al. (2021) suggested that some of the water molecules desorbed during daytime do not come down to the night side of the dawn terminator but move towards the day side, causing surficial and exospheric enhancements.

The diurnal variation of hydrogen with maximum concentration at lunar dawn and diminished concentration at lunar dusk, inferred from the Lunar Exploration Neutron Detector data (Livengood et al., 2015) also indirectly supports the present findings of density enhancement after sunrise, if the hydrogen be correlated to H_2O or OH. The decreasing number density of hydrogen at night time does not necessarily imply freezing/ adsorption of water. However, the thermal kinetic energy definitely decreases in absence of the sunshine and a major fraction of the particles fail to reach the altitude of the spacecraft. Further illustration with sample calculation of the most probable velocity during daytime is presented in the Discussion section.

3.2. Mid-latitude regions

Fig. 5 shows the diurnal variations of the abundance of H_2O and OH at a typical mid-latitude range (31° to 60° for both hemispheres) for varying solar longitudes. Similar to Fig. 1, the mean values and the ranges of variation are indicated by dots and straight lines, respectively. The enhancement of the number density after sunrise and the decrease of the same with sunset are faintly observed. The changes are not so regular as that of low latitudes [Fig. 4]. However, higher number density of both H_2O and OH are noted immediately after sunset, similar to that in Fig. 4. The post sunset and midnight abundances do not follow any regular trend.

The above characteristics of H_2O and OH may have different origins. The migration of exospheric molecules from the higher temperature

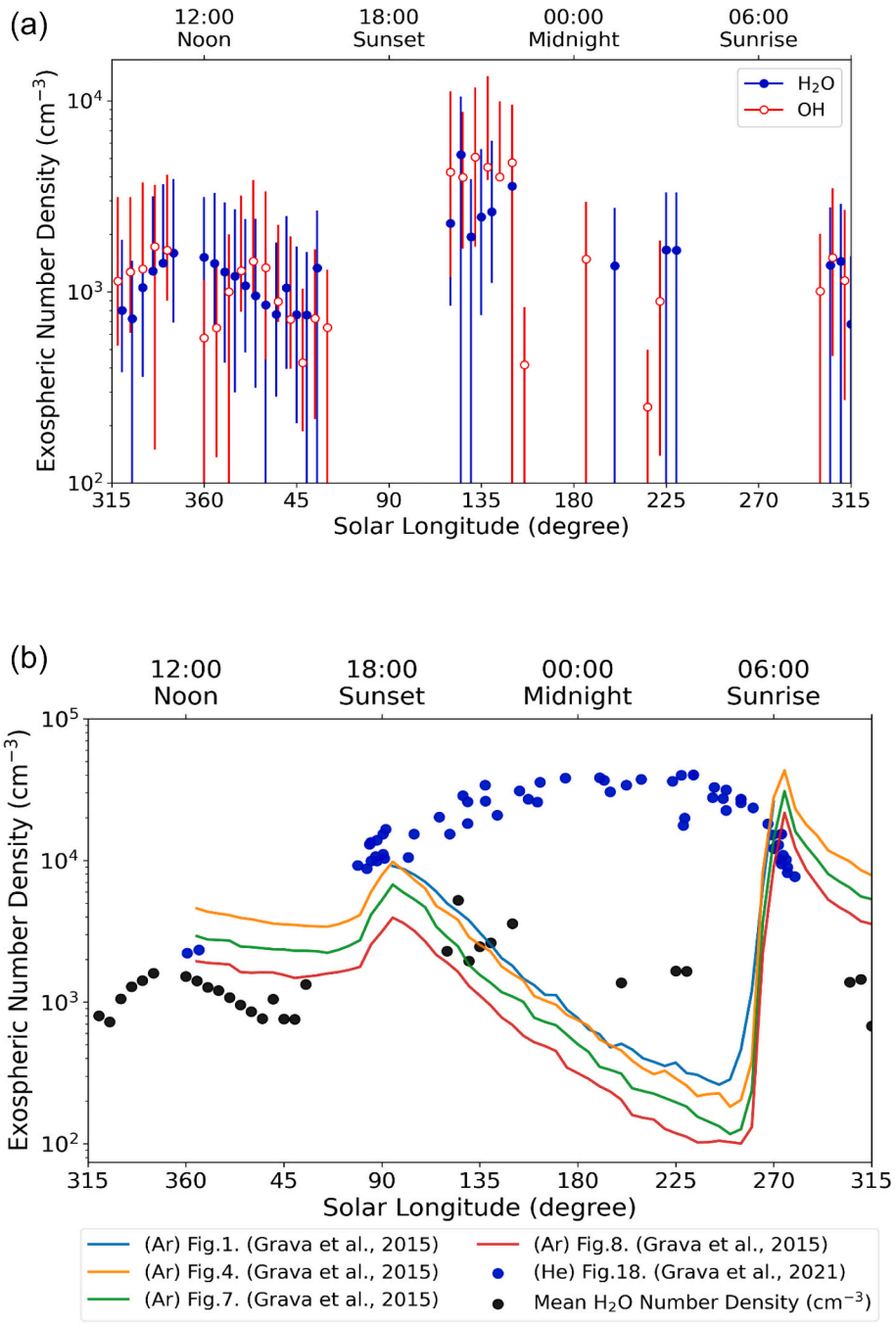

Fig. 4. (a). Number density of H_2O and OH at lunar exosphere for different solar longitudes for a typical low latitude range (0° to 30°). Solar longitude of 315°– 45°, 45°–135°, 135°–225° and 225°–315° represents noon, sunset, midnight, and sunrise respectively.
4(b). The expected local time trends of the number density of condensable (e.g. Ar) (Grava et al., 2015) and non-condensable (e.g. He) (Grava et al., 2021) species at lunar exosphere are obtained from literature and the same are compared with the mean H_2O density obtained from Fig. 4(a).

equatorial latitude to the lower temperature mid-latitude regions might have influenced the actual mass-spectroscopic information. Other possible reasons may be the latitude dependent rate of adsorption and desorption (Jones et al., 2018) or surface roughness effect (Prem et al., 2018).

3.3. High latitude regions

Fig. 6 depicts the diurnal variations of H_2O and OH abundance, at a typical high latitude range (61° to 80° for both hemispheres) for different solar longitudes. The latitudes greater than 80° were excluded because of less diurnal variation in surface temperature and a large difference in solar longitude out of a small change in location. Unfortunately, the full diurnal data, particularly that during noon and midnight are not available for the high latitudes. However, the post-sunrise (270° – 315°) data indicates a faint increasing trend for H_2O and the pre-sunset (45° – 90°) data indicate a weak decreasing tendency for the same, which are similar to the low-latitude and mid-latitude regions. The OH abundance is relatively higher at the sunrise terminator. A higher density of both H_2O and OH is noted immediately after sunset in high latitudes also, similar to that of low-latitude and mid-latitude regions. A possible reason may be the dissociation of H_2O to OH due to exposure to solar ultraviolet radiation during daytime.

At higher latitudes, the temperature variation is 260 K to 320 K as per

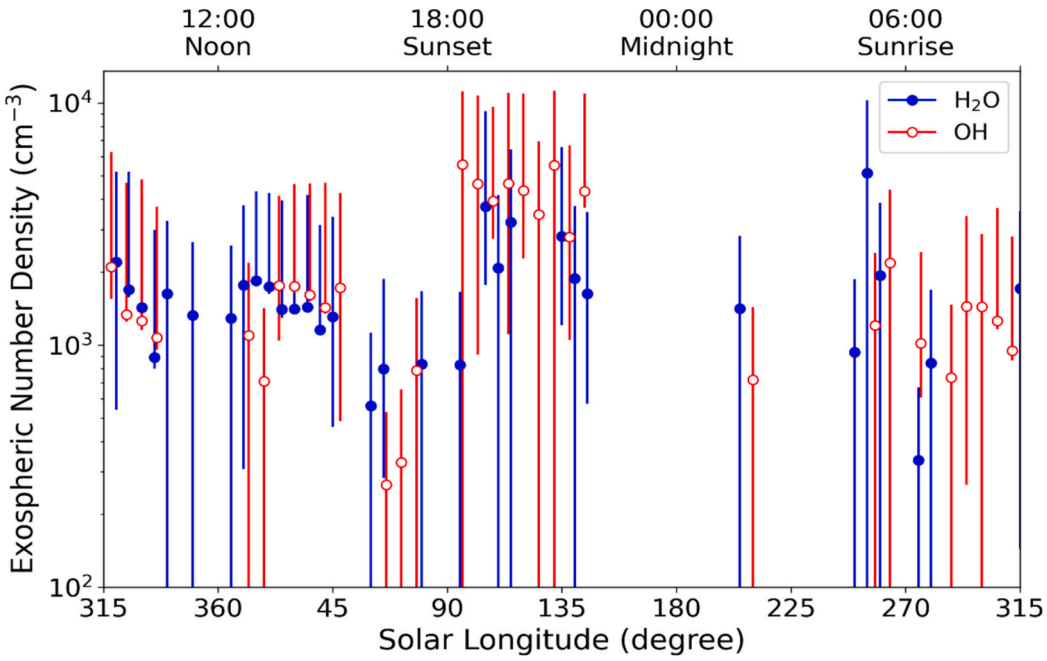

Fig. 5. Number density of H_2O and OH at lunar exosphere for different solar longitudes for a typical mid-latitude range (31° to 60°). Solar longitude of 315°– 45°, 45°–135°, 135°–225° and 225°–315° represents noon, sunset, midnight, and sunrise respectively.

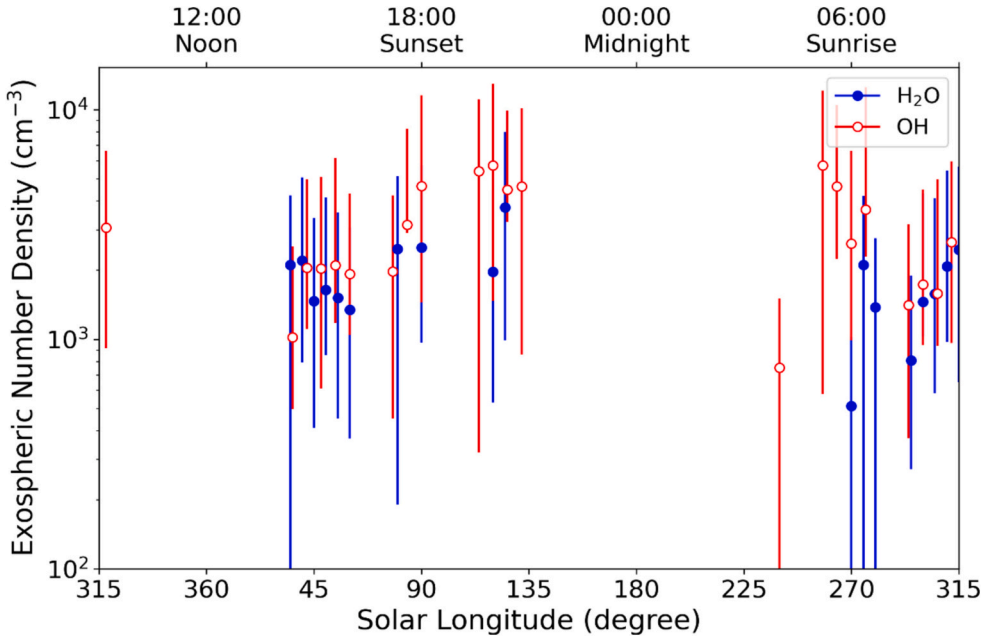

Fig. 6. Number density of H_2O and OH at lunar exosphere for different solar longitudes for a typical high latitude range (61° to 80°). Solar longitude of 315°– 45°, 45°–135°, 135°–225° and 225°–315° represents noon, sunset, midnight, and sunrise respectively.

Diviner radiometer measurement (Hurley et al., 2015). The diurnal variation due to solar insolation is not expected to be significant there. However overall, higher OH abundances at mid latitude and high latitude are sufficiently in agreement with the reported results (Honniball et al., 2022; Zhu et al., 2019; Tucker et al., 2019). Lunar Crater Observation and Sensing Satellite (LCROSS) observation shows sufficient ice signature within Cabeus crater (Colaprete et al., 2010) whereas Kaguya observation shows no water signature within Shackleton crater (Hayne et al., 2015). Therefore, it is very critical to comment about any particular location of abundance for ice and volatiles. Also, the permanently shaded areas may increase due to an enhanced shaded area during noon time, as the sun moves towards the local horizon. There may be self-shadowed areas as well as mutual shadowing due to the obstructions from other surface structures. These all give rise to different temperature signatures, which have significant impact on the stability of volatile like water.

Table 2 summarizes the maximum and minimum abundances obtained for H_2O and OH for the low, mid and high latitude regions illustrated above. The maximum number density of H_2O decreases on moving from lower to higher latitudes. The higher daytime temperatures at lower latitudes impart more ballistic throws to the molecules thereby increasing the detectable numbers from the spacecraft. The OH densities

Table 2
Spatiotemporal variations of H_2O and OH abundance at a glance, as measured by CHACE-2.

Latitude	Species	Number of Available Spectra (Ram Direction)	Latitude Range (°)	Maximum Number Density (cm^{-3})	Minimum Number Density (cm^{-3})
Low	H_2O	30	0 to 30	5225	678
	OH	29	0 to 30	5079	249
Mid	H_2O	32	31 to 60	5135	335
	OH	36	31 to 60	5565	265
High	H_2O	18	61 to 80	3747	511
	OH	22	61 to 80	5720	752

are comparable to that of H_2O except for at high latitudes where the OH shows an anomalous increase. Such diverse observations at different latitudinal regions of the lunar exosphere imply that the temperature variation is a major factor but may not be the single controlling one for the diurnally varying abundance of water group molecules. Therefore, the comparative results on the H_2O and OH abundance at lower and higher latitude regions and their diurnal variations may be useful for understanding the condensable nature of lunar water. Comparison of the daytime and the night time abundances can provide useful tool for tracking the absorption of molecules at lower temperature and subsequent desorption at higher temperatures and the consequent global recycling of the total water in the exosphere.

3.4. An integrated view

The above sections have analyzed the H_2O and OH diurnal abundances in the lunar exosphere separately for lower, middle and higher latitudinal regions. Now the overall characteristics are considered. Temperature program desorption experiments conducted with Apollo lunar samples under ultrahigh vacuum conditions inferred that highland samples adsorbed much more water (~30 %) than mare samples (Jones et al., 2020). Similar experiments found highland samples to retain much more (~40 times) water than mare samples and a significant probability of desorption over a lunar day was concluded (Poston et al., 2015). Considering such reports, it is quite logical to expect a higher concentration of H_2O at the 'sky' of highland regions during daytime. The passage of CHACE-2 in polar orbits is not restricted to near-

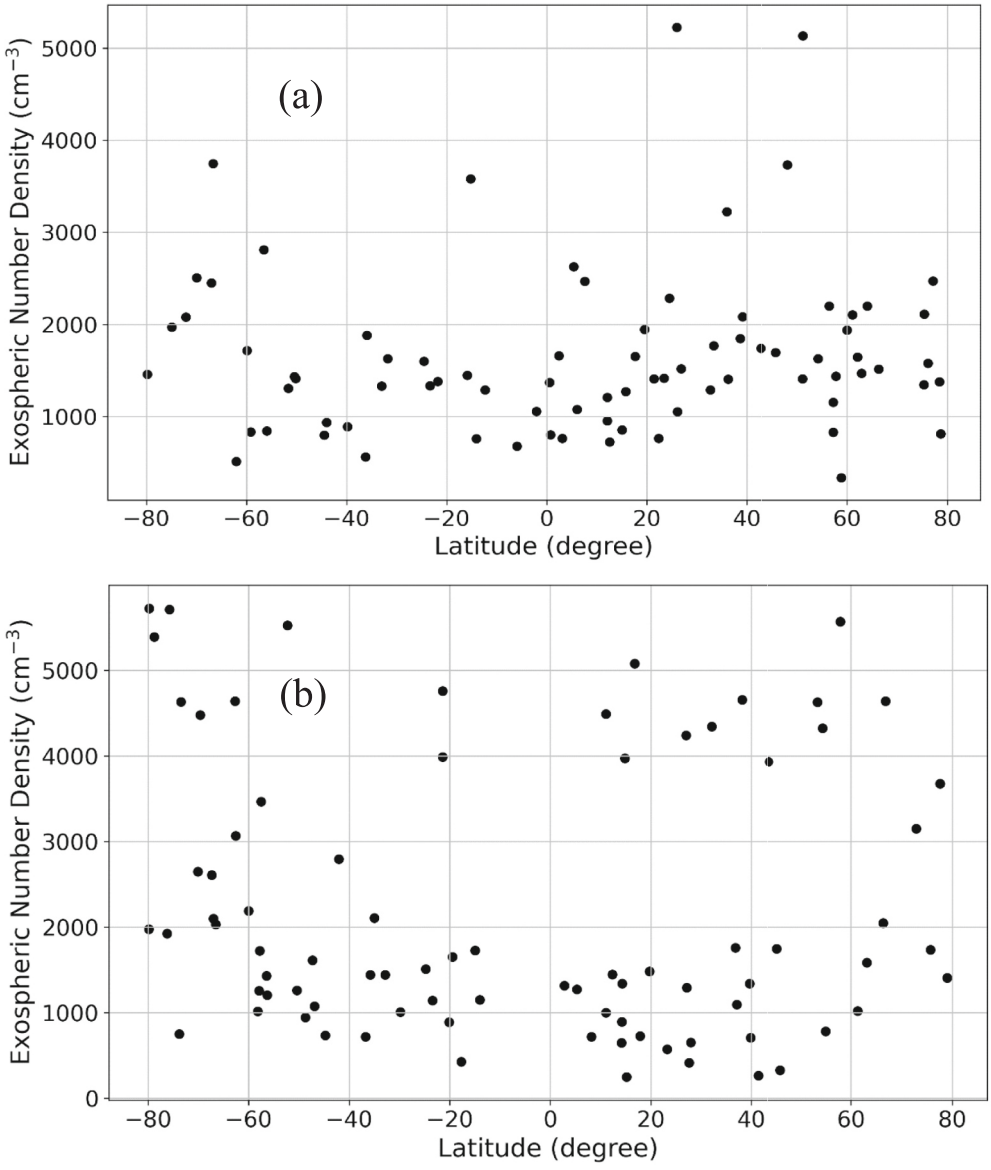

Fig. 7. Mapping the number density of (a) H_2O and (b) OH over gridded cells of latitude.

equatorial regions and it almost inevitably traces over the highland regions comprising many craters in and around (https://quickmap.lroc.asu.edu), which are unanimously considered as inventory for volatiles. Therefore, it is very likely that the abundance of water, as observed from exosphere is reasonably high at nearly 100 km altitude and this is the first observation where a high sensitivity and high-resolution mass spectrometer have identified separately the presence of molecular water and hydroxyl ion.

Summing up the results of Fig. 4(a), Fig. 5 and Fig. 6 and referring to Table 2, it is inferred that the H_2O abundances at the higher and lower latitudes are almost of the same order but there is a decreasing tendency towards higher latitudes. Fig. 7(a) and 7(b) present a comprehensive picture of the latitudinal variation of H_2O and OH, respectively, in both hemispheres. It is observed that the OH abundance is slightly higher than H_2O at all latitudes and has an increasing tendency towards higher latitude, which is partly in conformity with the concept of surface-trapped hydroxyl increasing with latitude (Honniball et al., 2022). It is worth mentioning that Honniball et al. (2022) showed that the ratio of exospheric to surface mass of water might vary over a wide range of 10^{-3} to 10^{-8}, if the activation energy of desorption increased by 0.3 eV. They attempted to quantify their SOFIA-measured results in terms of freely migratable adsorbed water but resulted in an extremely large exospheric density and negated the same adhering to the finding of Benna et al. (2019). Since the calculated results are so diverging and so sensitive to the reported values of activation energy that vary widely, it is not impossible to come up with the exospheric densities comparable to the present values. Some spot values are calculated below for comparing with the reported results.

Based on the maximum and minimum values of H_2O number density detected by CHACE-2 (Table 2) for low and mid-latitude regions, we assume a mean number density (n) of 2.78×10^3 cm^{-3} for H_2O at a height (h) of 100 km, comparable to CHACE-2 orbital height. Considering an average temperature (T) of 200 K and the standard values of Boltzmann constant (k_B), molecular mass of water (m) and lunar acceleration due to gravity (g), the scale height $\left(H = \frac{k_B T}{mg}\right)$ becomes ~56.84 km. Assuming hydrostatic equation $n = n_o exp\left(-\frac{h}{H}\right)$ to be valid for the lunar exosphere, the H_2O density (n_o) in the vicinity of ground level comes out to be $\sim 1.62 \times 10^4$ cm^{-3} so that the integrated column density (n_oH) is $\sim 9.21 \times 10^{10}$ cm^{-2}. The corresponding values for OH are $\sim 1.53 \times 10^4$ cm^{-3} and $\sim 9.21 \times 10^{10}$ cm^{-2}, respectively.

The above results are comparable with the estimates of Hendrix et al. (2019) where about 10^{12} cm^{-2} of H_2O molecules release into the lunar exosphere near local noon and about 40 % of those reaching the altitude of 50 km corresponds to roughly 400 cm^{-3}. Smolka et al. (2023) presented a simulation model for lunar exosphere and predicted H_2O surface density range of 5×10^3 to 4×10^5 cm^{-3}, which accommodates the present finding calculated above. Their predicted dayside surface density of OH ranges from 2.5×10^3 to 6.0×10^4 cm^{-3}, which matches literature values as well as the calculated values given above. Jones et al. (2024) modelled lunar water formation by recombinative desorption (RD) of surficial hydroxyls and micrometeoroid impacts (IM). The IM process was stated to produce higher amount of water at higher latitudes where RD was less active. The present results also find high densities of water at higher latitudes (Fig. 6), of the same order of that at lower latitudes [Fig. 4(a)]. Further elaborations on the reasonability of the present results are presented in the Discussion section.

3.5. Lunar passage through terrestrial geomagnetic tail

Though this topic is a bit deviated from the spatial and temporal variations of exospheric H_2O and OH, it investigates whether any potential origin of such variations can be established from this study. The solar wind interacts with the earth's magnetic field and deforms the magnetosphere. On the dayside, the magnetic field is compressed by the solar wind and on the night side, the magnetic field gets elongated as magnetotail along the direction of solar wind. The tail may extend up to more than 10^6 km and cover the Moon. The effect of magnetotail on the lunar exospheric tracers has been investigated since long time (Wilson et al., 2006; Das et al., 2017).

This work attempts to obtain information from CHACE-2 observations at the contrasting positions of absence and presence, respectively, of solar wind at lunar exosphere during the full moon (Sun-Moon distance ≈ Sun-Earth distance + Earth-Moon distance) and the new moon (Sun-Moon distance ≈ Sun-Earth distance – Earth-Moon distance) conditions. Several samples of partial pressure obtained during the occurrence and non-occurrence of magnetotail passage of the Moon are listed in Table 3. A significant and random variation of partial pressure (hence the number density) for H_2O is obtained there but no definite relationship with the presence or absence of magnetotail can be inferred therefrom. The suitability of CHACE-2 data for studying the magnetotail passage effect on water formation is not obvious here and it calls for further investigations.

4. Discussion

A common feature of the present results is much higher density of H_2O in comparison with others, such as LADEE (Benna et al., 2019). The rationality of the present results is put up in section 3.4 with exemplifying calculations and comparisons with the previous reports on inferred quantities, such as surface abundance and exospheric models.

Referring to Table 1 and comparing the features of CHACE-2 and LADEE NMS it is noted that CHACE-2 procured data over much longer duration and the data procured after a much longer initial time span (more than 1 year) were made into use in the present work so as to phase out the outgassing effect. LADEE NMS was confined to the near-equatorial regions of ±23° only and that too in varying orbit (~ 60 to 4 km) over a short time of few months. CHACE-2, being in polar orbit of ~100 km altitude, tracks from pole to pole and detects the local time variation of the exospheric species floating at different latitudes. The steady orbit of CHACE-2 has some other significance, as interpreted here.

The movement of the gas molecules in the lunar exosphere to be governed by the **k**inetic molecular theory of gases and Maxwell-Boltzmann distribution of velocity. The most probable velocity (v) is given by $\sqrt{\frac{2k_BT}{m}}$ where m is the molecular mass and T is the temperature. Therefore, the kinetic energy $\left(\frac{1}{2}mv^2\right)$ is given by k_BT. Kinetic theory implies that the particles have only kinetic energies and no potential energy. However, the lunar exosphere is gravitationally bound and we assume that the above kinetic energy holds the molecule at altitude h against gravity. Therefore, the potential energy (mgh) is equated to the

Table 3
Magnetotail passage information for amu 18.

Coordinated Universal Time (DD/MM/YYYY)	Roll Angle (°)	Partial Pressure ($\times 10^{-9}$ Torr) of amu 18	Magnetotail Passage
12/06/2022	0.3	8.7	Yes
13/06/2022	0	9.6	Yes
15/06/2022	0.1	6.16	Yes
05/01/2023	0.3	20.6	Yes
06/01/2023	0.1	14.8	Yes
07/01/2023	0.3	1.06	Yes
29/05/2022	0.3	5.99	No
30/05/2022	0.2	9.27	No
31/05/2022	0.1	12.2	No
20/01/2023	0.2	6.01	No
21/01/2023	0.3	10.1	No
22/01/2023	0.5	5.58	No

kinetic energy (k_BT) and the altitude (h) is calculated as $h = \frac{k_BT}{mg}$ with $k_B = 1.38 \times 10^{-23}$ m^2kgs^{-2} K^{-1}, $m = 29.9 \times 10^{-27}$ kg for water and $g = 1.625$ ms^{-2} for the Moon. The lunar temperature (T) is estimated by analytic approximation (Hurley et al., 2015). Two extreme values of temperature estimated with the present daytime data are 255.51 K and 382.75 K. The corresponding h values come out to be 72.57 km and 108.71 km, respectively, which match the CHACE-2 average orbiting height including the fluctuations. Earlier studies also report some results around the above ranges. For instance, in the Fig. 1 of Hurley et al. (2015), the green colour spanning 60° to 80° latitude indicates roughly 260 K to 320 K. Schörghofer et al. (2021) estimated a thermal ballistic hop distance of about 200 km for water molecules on the Moon. Thus, it is inferred that the most probable speed and the corresponding kinetic energy can haul the water molecules up to the heights comparable to the CHACE-2 orbit altitudes, at least in daytime so that the instrument detects the maximum number of molecules cluttered around this altitude. Consequently, a large number density is obtained.

Benna et al. (2019) obtained highly fluctuating data with the median density (22.8 cm^{-3}) comparable to the median absolute deviation (11.8 cm^{-3}). The present work also finds widely varying number densities (Figs. 4(a), 5 and 6) but over a larger range with mean of $\sim 10^3$ cm^{-3}. An interpretation of such fluctuations in both the cases can be put forward in terms of the most probable speed, i.e., the speed achieved by the largest fraction of the molecules. It corresponds to the kinetic energy possessed by most of the molecules. As the temperature increases after sunrise, the most probable speed, hence the kinetic energy of most of the molecules also increases but according to the basic law of kinetic molecular theory, the fractions of molecules possessing that kinetic energy get decreased. There occurs a wider range of speeds but fewer molecules possess the most probable speed. In other words, the probability of cluttering of molecules around a certain altitude is decreased. Such instability is likely to continue until the temperature increases further and becomes stable at noon. By that time, two different instruments: LADEE NMS at variable, lower orbit (~ 4–8 km, late in the mission) and CHACE-2 at fixed, higher orbit (~100 km) may record two different ranges of fluctuation.

Another notable feature of the present work is the distinction of H_2O and OH. CHACE-2, by virtue of its high resolution of 1 amu has been able to distinguish between H_2O (amu 18) and OH (amu 17). NMS, despite the same mass resolution was not decisive to resolve whether the original exospheric molecule was H_2O or OH because the incident hydroxyl radicals might have converted to H_2O by reacting with atomic hydrogen on the internal wall of the instrument. However, the chance of such a reaction is less for an open ion source instrument like CHACE-2. Some first-hand explanatory calculations are made in this connection in Appendix-I. This part also presents a potential explanation for the difference in the detected densities of H_2O and OH and the relatively higher abundance of OH.

5. Conclusion

Recent orbital and in situ measurements over the Moon have detected the presence of water or hydrated compounds in its surface and exosphere. However, there are wide deviations in the reported abundances of water, its spatial and temporal variations and the possible sources contributing to the lunar water. Such diversities motivated the authors to realize the significance of water in the Moon and to investigate the mass spectrometric data of CHACE-2, a payload of Chandrayaan-2, the second lunar mission of India.

This work has been able, for the first time, to distinguish between exospheric hydroxyl (OH) and molecular water (H_2O) from the partial pressure data and to explore the diurnal variations of these two entities in detail for equatorial (0° to 30°), mid-latitude (31° to 60°) and high latitude (61° to 80°) regions of both hemispheres for different solar time. For both H_2O and OH, there are indications of increased number density after sunrise and decrease of the same after noon, particularly at lower latitudes. Consistencies are noted with the reported chemical kinetic model for creation/loss of OH in lunar regolith and diurnal variations of hydrogen concentration. Interestingly, some discrete higher values of number density are noted after sunset also, mostly for OH. The diurnal asymmetry of temperature change may be a potential reason for sustaining the OH for a long time in the exosphere.

The present results do not infer any steady state exospheric water because both the H_2O and OH concentrations vary widely over latitudes and local time. However, a general finding is much higher density of H_2O at different latitudinal regions in comparison with the previous reports. A physics-based explanation is that the estimated lunar temperature can impart kinetic energy to water molecules so as to haul those up to the average height of CHACE-2. Since it is in polar orbit and its passage is traced through the highland regions, it can intercept the maximum number of molecules of the exosphere. Several spot values are calculated to demonstrate the reasonableness of the present results. A general inference is that the H_2O number densities are approximately of the same order in different latitudes but a decreasing tendency towards higher latitudes is indicated. Considering the overall latitudinal map, a greater abundance of OH is noted compared to that of H_2O, particularly at mid-latitudes and high latitudes. Temperature may be a major factor but not the only one for governing such spatial and temporal variations of water content in the exosphere. The dissimilar trends of H_2O and OH may have different origins, such as a finite time duration for dissociation, shadowing effects and surface roughness effects. There is possibility of dissociation of H_2O to OH in presence of ultraviolet radiation. The day-time and night-time solar longitudinal variations of H_2O and OH and their comparisons, similar to those executed in the present work can provide suitable means for tracing the adsorption of molecule at lower temperatures and subsequent desorption at higher temperatures and the consequent global water cycle in the exosphere.

CRediT authorship contribution statement

Swastika Chakraborty: Writing – original draft, Conceptualization. **Barun Raychaudhuri:** Writing – review & editing. **Tirtha Pratim Das:** Supervision, Project administration, Data curation. **Saurabh Das:** Supervision. **Moumita Roy:** Formal analysis.

Declaration of competing interest

The authors declare the following financial interests/personal relationships which may be considered as potential competing interests.

Swastika Chakraborty reports financial support was provided by Indian Space Research Organization.

Acknowledgements

This work is supported by Indian Space Research Organization, Department of Space, Government of India (ISRO/SPO/CH-2AO/2021-22). The significant technical support extended by CHANDRAYAAN-2 Mission Team is duly acknowledged.

Appendix A. Some relevant features of lunar water molecule (H_2O) and hydroxyl radical (OH)

Molecular water (H_2O) and hydroxyl radical (OH), both are asymmetric in three-dimensional structure. The hydroxyl may combine with another H^+ ion to form H–O–H, i.e. water molecule or with any other radical (R) to form another molecule (R–O–H). First, the distinguishability of H_2O and OH

in mass spectrometry with open ion source is discussed. Schörghofer et al. (2021) mentioned that the excess energy of dissociation of H_2O into H and OH imparted a mean velocity (v) of ~1 km s^{-1} to the OH and ~18 km s^{-1} to the H. The corresponding kinetic energy $\left(\frac{1}{2}mv^2\right)$ of OH, considering the molecular mass of 2.822×10^{-26} kg, comes out to be $\approx 1.41 \times 10^{-20}$ J. If the incident OH were to be converted to H_2O by reacting with atomic H on the interior wall of the instrument, this much energy would have to be supplied by some external agent. There is no solar ultraviolet radiation and only thermal energy $\left(\frac{3}{2}k_BT\right)$ within the instrument. Equating to the above value, the temperature becomes ≈680 K. Acquiring this much temperature in excess to the exospheric temperature common to all entities is quite unlikely. The whole open-source ionizer is within a vacuum ambient, similar to the exosphere itself. The ionizer filament temperature is, of course very high, of the order of ≈3000 K (Benna et al., 2019 Supplement) but the surrounding wall in vacuum cannot approach such a range. The situation is like a tungsten bulb filament and the surrounding glass bulb. Moreover, the heat of the inner walls may partly replenish the energy of the ingested water molecules lost by collisions with the walls. Thus, there is less chance of reactions on the interior walls of the instrument.

Next, an interpretation for the distinct spectral response of OH ions and H_2O molecules to infrared radiation of 3 and 6 μm reported in literature (Honniball et al., 2020; Honniball et al., 2022) is presented. Both H_2O and OH molecule may undergo rotation and/or vibration and each corresponds to some energy absorption. The rotation corresponds to much lower energy values and is not of the present interest. The vibrational movements can be stretching and bending, and the corresponding energy absorptions are in infrared range. The vibration may be asymmetric (when R is different from H) as well as symmetric (when R is same as H). However, the bending can occur with molecular water only and the corresponding energy is distinctly different. Following the report (Praprotnik et al., 2004), symmetric stretching appears at 3656 cm^{-1} or 2.735 μm, asymmetric stretching appears at 3755 cm^{-1} or 2.663 at μm and bending appears at 1594 cm^{-1} or 6.27 μm. Thus, both water molecules and hydroxyl compounds can respond to around 3 μm but it is only molecular water that responds to around 6 μm, corresponding to a lower energy.

Finally, a possible explanation is put up for the difference in the detected densities of H_2O and OH at a certain latitudinal span. In the exosphere, the collision among the molecules is negligible and each molecule can be treated individually. This does not rule out the possibility of collision with the infrared photons of the incident solar radiation. We consider an ideal case when the whole of the 6 μm and 3 μm photon energy get absorbed to the H_2O molecule and the OH ion, respectively. The photon momenta are negligibly small compared to the molecular momenta but both the 3 μm and 6 μm photon energies are distinctly larger than the thermal energy. Obeying the conservation of energy and momentum, the absorption of these photons might result in the speed of 2105 ms^{-1} and 1533 ms^{-1} for H_2O and OH, respectively. Such a difference of speed indicates that a lower energy may cause larger deviation to H_2O abundance at a certain place compared to that of OH, causing a difference in the local density.

Data availability

The authors do not have permission to share data.

References

Benaroya, H., 2017. Lunar habitats: a brief overview of issues and concepts. Reach 7, 14–33. https://doi.org/10.1016/j.reach.2018.08.002.

Benna, M., Hurley, D.M., Stubbs, T.J., Mahaffy, P.R., Elphic, R.C., 2019. Lunar soil hydration constrained by exospheric water liberated by meteoroid impacts. Nat. Geosci. 12, 333–338. https://doi.org/10.1038/s41561-019-0345-3.

Bhardwaj, A., et al., 2015. MENCA experiment aboard India's mars orbiter mission. Curr. Sci. 109 (6), 1106–1113. https://doi.org/10.18520/v109/i6/1106-1113.

Chauhan, P., et al., 2021. Unambiguous detection of OH and H_2O on the moon from Chandrayaan-2 imaging infrared spectrometer reflectance data using 3 μm hydration feature. Curr. Sci. 121 (3), 391–401. https://doi.org/10.18520/cs/v121/i3/391-401.

Clark, R.N., 2009. Detection of adsorbed water and hydroxyl on the moon. Science 326 (5952), 562–564. https://doi.org/10.1126/science.1178105.

Colaprete, A., et al., 2010. Detection of water in the LCROSS ejecta plume. Science 330 (6003), 463–468. https://doi.org/10.1126/science.1186986.

Crotts, A.P., Hummels, C., 2009. Lunar outgassing, transient phenomena and the return to the moon, II: predictions and test for outgassing and regolith interactions. Astrophys. J. 707, 1506–1523. https://doi.org/10.1088/0004-637X/707/2/1506.

Das, T.P., Thampi, S.V., Bhardwaj, A., Ahmed, S.M., Sridharan, R., 2016. Observation of Neon at mid and high latitudes in the sunlit lunar exosphere: results from CHACE aboard MIP/Chandrayaan-1. Icarus 272, 206–211. https://doi.org/10.1016/j.icarus.2016.02.030.

Das, T.P., Thampi, S.V., Dhanya, M.B., Bhardwaj, A., Ahmed, S.M., Sridharan, R., 2017. Upper limit of helium-4 in the sunlit lunar exosphere during magnetotail passage under low solar wind condition: result from CHACE aboard MIP in Chandrayaan-1. Icarus 297, 189–194. https://doi.org/10.1016/j.icarus.2017.07.001.

Das, T.P., et al., 2020. Chandra's atmospheric composition Explorer-2 onboard Chandrayaan-2 to study the lunar neutral exosphere. Curr. Sci. 118, 202. https://doi.org/10.18520/cs/v118/i2/202-209.

Dhanya, M.B., et al., 2021. Argon-40 in lunar exosphere: observations from CHACE-2 on Chandrayaan-2 orbiter. Geophys. Res. Lett. 48, e2021GL094970. https://doi.org/10.1029/2021GL094970.

Dhanya, M.B., Yadav, C.M., Thampi, S.V., Thampi, R.S., Das, T.P., 2023. Peak filter algorithm for the calibration of mass spectra from CHACE-2 aboard Chandrayaan-2 orbiter. Int. J. Mass Spectrom. 491, 117098. https://doi.org/10.1016/j.ijms.2023.117098.

Elphic, R.C., et al., 2014. The lunar atmosphere and dust environment explorer Mission. Space Sci. Rev. 185, 3–25. https://doi.org/10.1007/s11214-014-0113-z.

Grava, C., et al., 2015. Lunar exospheric argon modeling. Icarus 255, 135–147. https://doi.org/10.1016/j.icarus.2014.09.029.

Grava, C., et al., 2021. LRO/LAMP observations of the lunar helium exosphere: constraints on thermal accommodation and outgassing rate. Mon. Not. R. Astron. Soc. 501 (3), 4438–4451. https://doi.org/10.1093/mnras/staa3884.

Hayne, P.O., et al., 2015. Evidence for exposed water ice in the Moon's south polar regions from lunar reconnaissance orbiter ultraviolet albedo and temperature measurements. Icarus 255, 58–69. https://doi.org/10.1016/j.icarus.2015.03.032.

Hendrix, A.R., et al., 2019. Diurnally-migrating lunar water: evidence from ultraviolet data. Geophys. Res. Lett. 46 (5), 2417–2424. https://doi.org/10.1029/2018GL081821.

Honniball, C.I., et al., 2020. Telescopic observations of lunar hydration: variations and abundance. J. Geophys. Res.: Planets 125 (9). https://doi.org/10.1029/2020JE006484 p.e2020JE006484.

Honniball, C.I., et al., 2021. Molecular water detected on the sunlit moon by SOFIA. Nat. Astronom. 5 (2), 121–127. https://doi.org/10.1038/s41550-020-01222-x.

Honniball, C.I., Lucey, P.G., Arredondo, A., Reach, W.T., Malaret, E.R., 2022. Regional map of molecular water at high southern latitudes on the moon using 6 μm data from the stratospheric Observatory for Infrared Astronomy. Geophys. Res. Lett. 49 (9). https://doi.org/10.1029/2022GL097786 p.e2022GL097786.

Huicun, He, et al., 2023. A solar wind-derived water reservoir on the moon hosted by impact glass beads. Nat. Geosci. 16 (4), 294–300. https://doi.org/10.1038/s41561-023-01159-6.

Hurley, D.M., et al., 2015. An analytic function of lunar surface temperature for exospheric modelling. Icarus 255, 159–163. https://doi.org/10.1016/j.icarus.2014.08.043.

Ibánez, M., Dieball, C., Lasanta, A., Godec, A., Rica, R.A., 2024. Heating and cooling are fundamentally asymmetric and evolve along distinct pathways. Nat. Phys. 20 (1), 135–141. https://doi.org/10.1038/s41567-023-02269-z.

Jones, B.M., Aleksandrov, A., Hibbitts, K., Dyar, M.D., Orlando, T.M., 2018. Solar wind-induced water cycle on the moon. Geophys. Res. Lett. 45 (20), 10,959–10,967. https://doi.org/10.1029/2018GL080008.

Jones, B.M., Aleksandrov, A., Dyar, M.D., Hibbitts, C.A., Orlando, T.M., 2020. Investigation of water interactions with Apollo lunar regolith grains. J. Geophys. Res. Planets 125 (6). https://doi.org/10.1029/2019JE006147 p.e2019JE006147.

Jones, B.M., Carrillo-Sánchez, J.D., Janches, D., Sarantos, M., Orlando, T.M., 2024. Water generation on the moon from solar wind and meteoroid impacts. Planeta. Sci. J. 5 (8). https://doi.org/10.3847/PSJ/ad5542, 171 (26pp).

Lawrence, D.J., Peplowski, P.N., Wilson, J.T., Elphic, R.C., 2022. Global hydrogen abundances on the lunar surface. J. Geophys. Res. Planet. 127 (7), e2022JE007197. https://doi.org/10.1029/2022JE007197.

Li, S., Milliken, R.E., 2017. Water on the surface of the moon as seen by the moon mineralogy mapper: distribution, abundance, and origins. Sci. Adv. 3 (9), e1701471. https://doi.org/10.1126/sciadv.1701471.

Livengood, T.A., et al., 2015. Moonshine: diurnally varying hydration through natural distillation on the moon, detected by the lunar exploration neutron detector (LEND). Icarus 255, 100–115. https://doi.org/10.1016/j.icarus.2015.04.004.

Mahaffy, P.R., et al., 2014. The neutral mass spectrometer on the lunar atmosphere and dust environment explorer mission. In: The Lunar Atmosphere and Dust

Environment Explorer Mission (LADEE), pp. 27–61. https://doi.org/10.1007/978-3-319-18717-4_3.
Pieters, C.M., et al., 2009. Character and spatial distribution of OH/H_2O on the surface of the moon seen by M3 on Chandrayaan-1. Science. https://doi.org/10.1126/Science.1178658.
Poston, M.J., Grieves, G.A., Aleksandrov, A.B., Hibbitts, C.A., Dyar, M.D., Orlando, T.M., 2015. Temperature programmed desorption studies of water interactions with Apollo lunar samples 12001 and 72501. Icarus 255, 24–29. https://doi.org/10.1016/j.icarus.2014.09.049.
Praprotnik, M., Janežič, D., Mavri, J., 2004. Temperature dependence of water vibrational spectrum: a molecular dynamics simulation study. J. Phys. Chem. A 108 (50), 11056–11062. https://doi.org/10.1021/jp046158d.
Prem, P., Goldstein, D.B., Varghese, P.L., Trafton, L.M., 2018. The influence of surface roughness on volatile transport on the moon. Icarus 299, 31–45. https://doi.org/10.1016/j.icarus.2017.07.010.
Sarantos, M., Killen, R.M., Glenar, D.A., Benna, M., Stubbs, T.J., 2012. Metallic species, oxygen and silicon in the lunar exosphere: upper limits and prospects for LADEE measurements. J. Geophys. Res. Space Physics 117 (A3). https://doi.org/10.1029/2011JA017044.
Schläppi, B., et al., 2011, December. Characterization of the gaseous spacecraft environment of Rosetta by ROSINA. In: 3rd AIAA Atmospheric Space Environments Conference, p. 3822. https://doi.org/10.2514/6.2011-3822.
Schörghofer, N., et al., 2021. Water group exospheres and surface interactions on the moon, mercury, and Ceres. Space Sci. Rev. 217 (6), 74. https://doi.org/10.1007/s11214-021-00846-3.
Shearer, C.K., et al., 2006. Thermal and magmatic evolution of the moon. Rev. Mineral. Geochem. 60 (1), 365–518. https://doi.org/10.2138/rmg.2006.60.4.
Smolka, A., Nikolić, D., Gscheidle, C., Reiss, P., 2023. Coupled H, H_2, OH, and H_2O lunar exosphere simulation framework and impacts of conversion reactions. Icarus 397, 115508. https://doi.org/10.1016/j.icarus.2023.115508.
Sridharan, R., et al., 2010. The sunlit lunar atmosphere: a comprehensive study by CHACE on the moon impact probe of Chandrayaan-1. Planet. Space Sci. 58 (12), 1567–1577. https://doi.org/10.1016/j.pss.2010.07.027.
Sridharan, R., et al., 2015. Corrigendum to “the sunlit lunar atmosphere: a comprehensive study by CHACE on the moon impact probe of Chandrayaan-1” [planet. Space Sci. 58 (2010) 1567–1577]. Planet. Space Sci. 111, 167–168. https://doi.org/10.1016/j.pss.2014.12.021.
Tucker, O.J., Farrell, W.M., Killen, R.M., Hurley, D.M., 2019. Solar wind implantation into the lunar regolith: Monte Carlo simulations of H retention in a surface with defects and the H_2 exosphere. J. Geophys. Res.: Planet. 124 (2), 278–293. https://doi.org/10.1029/2018JE005805.
Watson, K., Murray, B., Brown, H., 1961a. On the possible presence of ice on the moon. J. Geophys. Res. 66 (5), 1598–1600. https://doi.org/10.1029/JZ066i005p01598.
Watson, K., Murray, B.C., Brown, H., 1961b. The behaviour of volatiles on the lunar surface. J. Geophys. Res. 66 (9), 3033–3045. https://doi.org/10.1029/JZ066i009p03033.
Williams, J.-P., Paige, D.A., Greenhagen, B.T., Sefton-Nash, E., 2017. The global surface temperatures of the moon as measured by the diviner lunar radiometer experiment. Icarus 283, 300–325. https://doi.org/10.1016/j.icarus.2016.08.012.
Wilson, J.K., Mendillo, M., Spence, H.E., 2006. Magnetospheric influence on the Moon’s exosphere. J. Geophys. Res. Space Physics 111 (A7). https://doi.org/10.1029/2005JA011364.
Wöhler, C., Grumpe, A., Berezhnoy, A.A., Shevchenko, V.V., 2017. Time-of-day–dependent global distribution of lunar surficial water/hydroxyl. Sci. Adv. 3 (9), e1701286. https://doi.org/10.1126/sciadv.1701286.
Zhu, C., et al., 2019. Untangling the formation and liberation of water in the lunar regolith. Proc. Natl. Acad. Sci. 116 (23), 11165–11170. https://doi.org/10.1073/pnas.1819600116.